Soft Condensation

Ambre Bouillant,[1,2] Christopher Henkel,[3] Uwe Thiele,[3] Bruno Andreotti,[4] and Jacco H. Snoeijer[1]
[1]Physics of Fluids Group, University of Twente, 7500 AE Enschede, Netherlands
[2]MSC, UMR 7057 CNRS, UPC, 10 rue Alice Domon et Léonie Duquet, 75013 Paris, France
[3]Institut für Theoretische Physik, Universität Münster, Wilhelm-Klemm-Straße 9, 48149 Münster, Germany
[4]LPENS, UMR 8550 CNRS, ENS, UPCité, SU, 24 rue Lhomond, 75005 Paris, France

(Received 9 July 2024; revised 5 February 2025; accepted 11 April 2025; published 9 May 2025)

When moist air meets a cold surface, it creates a breath figure characterized by numerous small droplets. The central question is how the vapor flux is distributed between the growth of condensed drops and the nucleation of new ones. Here, we investigate the nucleation, growth, and coalescence of droplets on soft substrates consisting of cross-linked polymer networks. The number of droplets initially remains constant, until drops start to coarsen according to a universal law; both phenomena are explained via the formation of a saturated boundary layer. We quantitatively unveil an algebraic sensitivity of the number of droplets on substrate elasticity, which is unexpected since nucleation occurs at a scale where the polymer network resembles a melt. Breath figures thus offer a macroscopic probe of the molecular characteristics of the polymer surface, and suggest a surprisingly low-energy pathway for nucleation.

DOI: 10.1103/PhysRevLett.134.188204

When humid air is directed onto a mirror, a fine mist of water droplets condenses on its surface. This process involves *nucleation*, the emergence of nascent structures of a new phase, that is prevalent in nature, and is fundamental across various domains including cloud condensation, cell biology, material sciences, food industry, and water collection [1,2]. The patterns formed by dew on a substrate, known as "breath figures" [3], have been thoroughly investigated on various substrate types [4,5], from rough [6,7], chemically heterogeneous or patterned [8,9], polymeric [10–15], liquid-infused [16,17] to pure liquid substrates [18,19]. The collected droplets typically evolve towards scale-free size distributions, ranging from freshly nucleated nanometer-scale drops to millimeter sizes after growth and coalescence [15,20–26]. A remarkable unexplained feature is that on atomically smooth substrates, the droplet patterns initially appear to be nearly monodisperse [18,19], as if all drops appeared simultaneously through a single nucleation burst.

Highly deformable polymer networks allow us to modify surface wettability and droplet interactions [13,27,28], which may be exploited for condensation-based patterning applications [29–33]. Recent studies have resolved the long-standing question of how sessile, isolated, macroscopic drops wet soft elastic surfaces [34]. The equilibrium shape of isolated sessile macroscopic drop is dictated by the elasto-capillary length γ/G, which compares the surface tension γ with the substrate elastic shear modulus G. Droplets smaller than γ/G sink into the substrate to form liquid lenses. Nearby drops interact through substrate-mediated elastocapillary deformations, an effect known as the inverted "Cheerios effect" [28]. Whether the classical elastocapillary framework accurately describes the key features of soft condensation, from the nucleation of isolated nanodroplets to collective effects, remains an open question that we address here.

In this Letter, we experimentally investigate the condensation of water vapor on soft polymeric substrates with elastic moduli $G \in [10^2; 10^6]$ Pa. Figure 1 shows that the

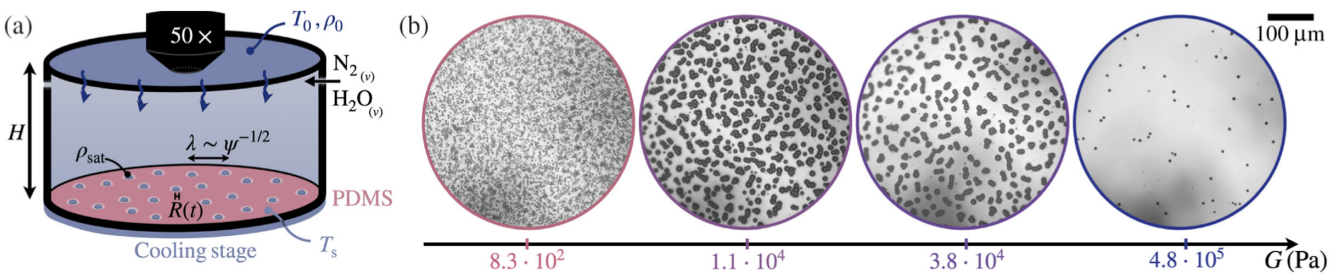

FIG. 1. (a) Schematic of the controlled humidity chamber. (b) Breath figures imaged from above using a microscope, on substrates of increasing elastic modulus G for $\rho/\rho_{sat}(T_s) = 1.22 \pm 0.11$.

number of droplets that condense varies dramatically upon changing the substrate stiffness. This observation cannot at all be explained by the elastocapillary framework, which predicts nanometric nuclei to be insensitive to the degree of reticulation, since their size is much smaller than γ/G. A central result is that, in contrast to previous studies, the distribution of drop sizes is nearly monodisperse and the nucleation has completely stopped once drops reach the optically accessible range of a few microns. We develop a quantitative model that explains the arrest of nucleation, and the subsequent growth and coarsening, offering a route towards the actual rate of nucleation at the nanoscale.

Experimental setup—Materials and methods are detailed in the Supplemental Material (SM) [35]. We prepare millimeter-thick soft reticulated polymer networks by premixing and curing silicone (Dow Corning; Sylgard 184) with its reticulant agent in weight proportions ranging from 10∶1 up to 80∶1 (extending the range in [36]) or the two prepolymer components (DowCorning; CY52-276 A∶B, in relative proportions 1.3∶1 and 1∶1 & Zhermack; PVS Elite Double 8 elastomer, mixing the two components in equal proportion.). Tuning the ratio of base polymer to cross-linker, the elastic modulus $G \in [10^2\text{–}10^6]$ Pa, while keeping the same chemical composition. It should be noted that several properties, such as the density of dangling ends or cross-linkers and the residual melt inside the network, vary simultaneously. In the remainder, we use G to label the tested substrates as it provides more insight than the base polymer to cross-linker mass ratio r and can be measured unequivocally. The results presented here are similar whether uncross-linked polymer chains are extracted or not (cf. SM [35]). Experiments are also performed on a stiff PDMS pseudo-brush (cf. [35] [37,38]); drops cannot sink into these substrates and thus form spherical caps of contact angle $\theta_{\text{brush}} = 100 \pm 5°$. The low G limit is probed by experiments on uncrosslinked PDMS melt. Macroscopic drops on all tested substrates exhibit no contact angle hysteresis or pinning. Defects are ruled out as drops do not form at the same locations in successive experiments.

The condensation is driven by supersaturation that leads to a difference in chemical potential $\Delta\mu = -k_B T \ln(\rho/\rho_{\text{sat}})$ between the liquid and vapor phase, where ρ is the water vapor mass per unit volume and ρ_{sat} its saturation value. Experiments are performed in a closed cell of height $H = 42$ mm equipped with a controlled humid or dry air inlet that maintains humidity $\rho = \rho_0$ constant at the ceiling, maintained at temperature $T_0 = 22 \pm 4$ °C [Fig. 1(a)]. The substrate is placed on a cooling Peltier stage at the bottom of the chamber. Quenching the substrate temperature to $T_s = 5 \pm 1$ °C in a few seconds triggers the nucleation and growth of nanometric dew drops on the substrate. The breath figures are illuminated and recorded from above with a Nikon camera (D850) mounted on an upright Olympus microscope with ×50 magnification. This yields a spatial resolution of 12 pixels/μm, allowing for the detection of droplets once their size reaches the micron scale.

Number of drops—Figure 1(b) shows typical dew patterns. Changing the degree of reticulation of the polymer network dramatically affects drop density: softer substrates clearly favor nucleation as first noted by [13] and also observed on relatively stiff substrates by [14]. In stark contrast with [15,20–22,24–26], the distribution of drop sizes is nearly monodisperse [Fig. 1(b)] and almost no new drops form, at least after they reach the visible micron scale. During a time ranging from 10^2–10^3 s, the number of drops per unit area ψ_0 remains constant, while drops increase in volume (cf. raw data in Figs. S7–S9 [35]). Figure 2 shows that the drop surface density ψ_0 presents an algebraic dependence on G between the two limiting cases of the uncross-linked melt (yellow symbol) and the stiff brush (black symbol). Note the much broader range of G than in [14].

Figure 3 shows that after some time, the drop pattern exhibits a universal coarsening where the density ψ decreases in times as $\psi \sim t^{-2}$. In a companion paper [39], a geometrical argument is presented to derive the law obeyed by the droplet density $\psi(t)$ during coalescence:

$$\psi = \frac{\psi_0}{(1 + (t - \tau_p)/\tau_c)^2}, \qquad \tau_c^{\text{th}} \sim \frac{\rho_\ell H}{\psi_0^{1/2} D(\rho_0 - \rho_{\text{sat}})}, \quad (1)$$

which is the red line in Fig. 3(c). The predicted coarsening time τ_c^{th} involves the diffusion constant of water vapor in air $D = 2.3 \times 10^{-5}$ m^2/s. On stiff substrates, the coalescence between two contacting drops is nearly instantaneous ($\tau_p \approx 0$) [Fig. 3(a)]. On soft substrates, however, droplets display a foamlike structure that resists coalescence [Fig. 3(b)] and exhibits an Ostwald-like ripening process. Still, the evolution of $\psi(t)$ is observed to follow the same law, albeit with a significant delay time τ_p before

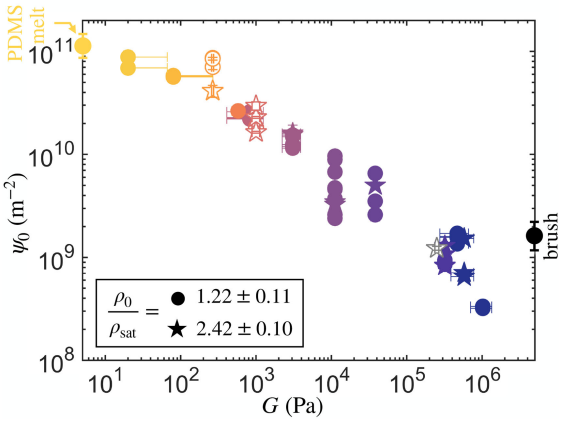

FIG. 2. Drop initial surface density ψ_0 measured once drops become visible ($R \sim 1$ μm) as a function of G. Values for PDMS melt and stiff brush are also reported.

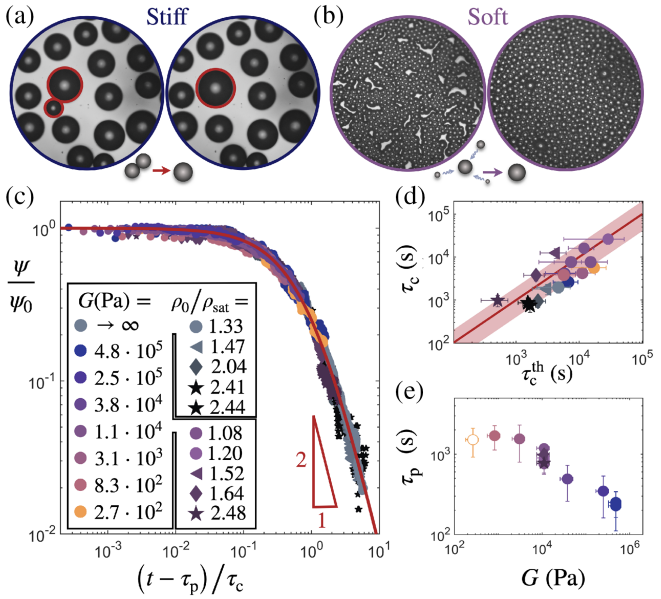

FIG. 3. Evolution of breath figures (seen from top) on (a) brush PDMS (before and after a merging event) (b) and a soft gel ($G = 1.1 \times 10^4$ Pa). (c) Normalized drop surface density ψ/ψ_0 for all tested substrates and humidities, as a function of rescaled time $(t-\tau_p)/\tau_c$. The coarsening time τ_c and delay time τ_p are deduced by fitting (1). (d) τ_c follows (1). The red line has a slope 1 ± 0.8. (e) τ_p corresponds to the plateau of $\psi(t)$, plotted as a function of the softness G. Raw data and the fits are shown in Figs. S7–S9 of SM [35].

coarsening starts [Fig. 3(e)]. This delay is only observed on viscoelastic substrates; it vanishes on stiff PDMS or after extracting the free chains (cf. SM [35,40]). The fitted coarsening time τ_c agrees well with prediction (1), for all tested substrates and humidities [Fig. 3(d)].

The key questions to address are why the number of droplets varies so strongly with softness, and why hardly any new drops are seen to nucleate during the experiment—leading to quasimonodisperse patterns. The latter observation is striking since nucleation is stochastic, with a nucleation rate J per unit surface that increases with the degree of supersaturation. The number of nucleated drops thus increases as $\psi \sim Jt$ during the initial stages of the experiment, at scales below optical resolution. In a companion paper [39], we show how vapor-mediated interactions between neighboring drops lead to a complete nucleation arrest. Below we leverage this result to relate the actual microscopic nucleation rate J to the experimentally measurable ψ_0 on soft gels.

Relating ψ_0 and the nucleation rate—The interaction between drops can be understood as follows. Initially, the typical distance between drops, $\psi^{-1/2}$, is much larger than their average radius, R [Fig. 1(a)]. Hence, the drops can be considered isolated and grow according to [5]

$$R^2 \sim D(\rho_0 - \rho_{sat})t/\rho_\ell, \tag{2}$$

where $\rho_\ell = 10^3$ kg/m^3. As drops grow, collective effects slow down this condensation dynamics [21,41]. Indeed, droplets are saturated at their liquid-vapor interface and thereby decrease the local humidity around them. We show in the companion paper [39] using a matched asymptotics description of the diffusion problem that the drops gradually build up a boundary layer: seen from the scale of the cell, the substrate becomes saturated at an effective humidity ρ_{eff},

$$\rho_{eff} = \frac{\rho_0 + 2\pi\mathcal{F}\psi RH\rho_{sat}}{1 + 2\pi\mathcal{F}\psi RH}, \tag{3}$$

where $\mathcal{F}$ is a known factor that accounts for the drop geometry [42].

Equation (3) reveals two distinct regimes, governed by the newly identified dimensionless parameter ψRH. In the early stage of condensation, that is, in the low density limit, $\psi RH \ll 1$, the effective humidity $\rho_{eff} \approx \rho_0$. Dew droplets thus initially grow according to (2). Conversely, in the high density limit, $\psi RH \gg 1$, the effective humidity at the substrate is well below ρ_0 and approaches ρ_{sat}. Since $\psi RH \sim 10^2$ when droplets become first visible, our experiments are in this high-density regime. Hence $\rho_{eff} \approx \rho_{sat}$ near the substrate, which explains why the nucleation of new droplets is arrested. The time of arrest τ_a is given by the crossover between the two regimes and can be determined from $\psi \sim Jt$ combined with (2) and (3). This selects the number of drops

$$\psi_0 \sim J\tau_a \sim \left(\frac{J}{H^2 D(\rho_0 - \rho_{sat})}\right)^{1/3}, \tag{4}$$

as is validated by stochastic numerics in [39]. This scenario explains why in experiments, for which $t \gg \tau_a$, it appears as if all drops nucleated quasisimultaneously.

Our saturation scenario can be tested experimentally. The diffusive flux across the cell saturates to $D(\rho_0 - \rho_{sat})/H$, and each drop receives a fraction of this flux. The average drop volume V is thus expected to grow as (see also [5]):

$$V = \frac{D(\rho_0 - \rho_{sat})}{\rho_\ell H}\frac{t}{\psi}. \tag{5}$$

Figure 4 shows that this linear growth of the volume is observed for all substrates, with a perfect match of the independently calibrated prefactor for the brush substrates. Quantitative analysis requires the conversion of the measured mean radius R to the mean drop volume. To that end, we introduce a geometrical factor $g \equiv V/R^3$, discussed in SM [35]. On brush substrates, drops form spherical caps of constant contact angle, allowing for an independent calibration $g = 2.6 \pm 0.4$ (cf. SM [35]). Data for the brush indeed follow (5) without any adjustable parameter. On soft

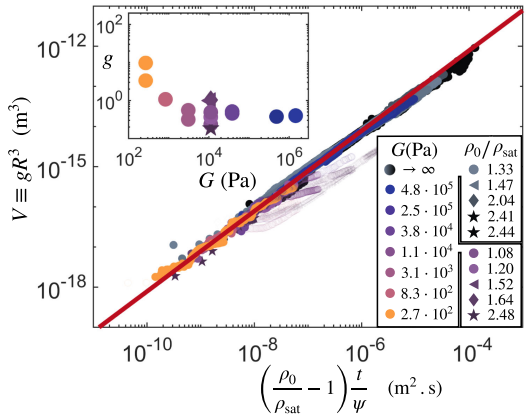

FIG. 4. Mean drop volume $V \equiv gR^3$ as a function of time rescaled according to Eq. (5) (red line) obtained on brush and soft substrates for various relative humidities ρ_0/ρ_{sat} and moduli G. For brushes, the geometrical factor $g = 2.6 \pm 0.4$ can be measured independently; for soft gels, g is left as a free parameter and its fitted value is reported in the inset as a function of G, excluding late-time transparent points, where drop sinking causes deviations from the linear trend. Raw data and fits are presented in SM [35].

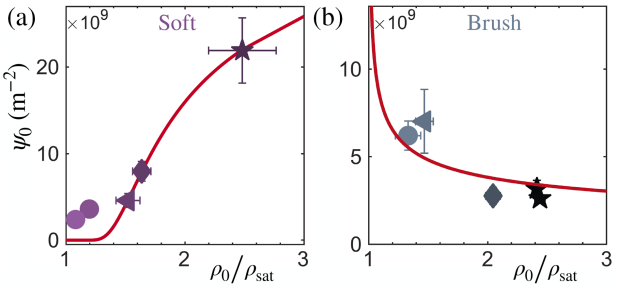

FIG. 5. Drop density ψ_0 as a function of ρ_0/ρ_{sat} measured on (a) soft PDMS gels ($G = 1.1 \times 10^4$ Pa) and on (b) PDMS brushes. Red lines are the best fits using (4), (6) (fitted values $\chi = 1.3$, $J_0 = 3.5 \times 10^{15}$ m^{-2} s^{-1}, and $\chi = 0$, $J_0 = 2.9 \times 10^{12}$ m^{-2} s^{-1}).

gels, drops partly sink into their substrate with a slow relaxation dynamics, which affect the contact angles in a nontrivial manner (cf. SM [35]), making the theoretical prediction of g intricate. Still, the scaling $R^3 \sim t/\psi$ is seen to hold. The value of g that is here fitted is found to decrease with G when $G < 3 \times 10^3$ Pa, reaching a plateau when $G > 3 \times 10^3$ Pa (Fig. 4, inset). At later times, the measured R^3 for very soft gels systematically fall below the linear prediction (Fig. 4, light points). This trend arises from drops geometrical adaptation with time (cf. SM [35]), and, in particular, to their sinking into the gel, storing part of their volume below the surface.

Discussion—The main unexplained experimental observation is that breath figures are much denser when the substrate is softer. This contradicts elastocapillary theory, which predicts the barrier for nanoscopic drops to be insensitive to the substrate's elasticity. Paradoxically, fewer and more widely spaced cross-links (cf. SM [35]) result in a higher number of nucleated droplets, ruling out the possibility that cross-links serve as nucleation-promoting heterogeneous sites. To gain further insight in the nucleation process, we consider the effect of humidity on the selected drop count ψ_0 in Fig. 5 and interpret the results in terms of classical nucleation theory (CNT). While for the gel ψ_0 increases with ρ/ρ_{sat} (panel a), a decrease is observed for breath figures on a brush (panel b). To explain these opposing trends, we use the connection between ψ_0 and J set by (4) [39], in conjunction with CNT

$$J = J_0 \exp\left(-\frac{\Delta\Phi^*}{k_B T}\right), \quad \text{with} \quad \Delta\Phi^* = \frac{\chi k_B T}{\ln^2(\rho/\rho_{sat})}, \quad (6)$$

describing nucleation as an activated process [5]. The energy barrier $\Delta\Phi^*$ is expected to decrease with ρ/ρ_{sat}, naturally giving an increase of nucleated drops with supersaturation. However, the explicit dependence on ρ/ρ_{sat} in (4), originating from the diffusive saturation mechanism, also admits the opposite trend. Indeed, both datasets in Fig. 5 can be fitted using (4), (6), as shown by the solid lines. For the soft gel, the best fit yields a normalized energy barrier $\chi = 1.3$, which is far below the macroscopic prediction of $\chi = 40 \pm 6$ (cf. SM [35]). A macroscopic description of nucleation thus results in a huge barrier within the exponential in (6). With a rescaled energy gap of $\chi = 40$ and even using the upper bound for J_0 (given by the flux of water molecules impacting the substrate), the estimated nucleation rate would be more than 300 orders of magnitude smaller than observed, implying no drops should be seen. Such a barrier is neither compatible with the moderate increase of ψ_0 with humidity observed experimentally. The failure of the macroscopic prediction for the barrier is even more striking for brushes, for which the number of drops decreases with humidity. The fit corresponds to $\chi = 0$, instead of the expected $\chi = 59 \pm 6$ (cf. SM [35]). As in many other nucleation problems [2,43,44], the so-called classical macroscopic nucleation theory is contradicted by the experiments. Our findings show that nucleation occurs via a microscopic path with a very low barrier, at most of a few $k_B T$ in dimensional units, which is very sensitive to the degree of reticulation.

Finally, we found that breath figures on various soft PDMS substrates exhibit a nearly monodisperse distribution, even during the later coalescence stage, in contrast with most literature on dew formation. This observation is explained quantitatively by the theory developed in [39] and is attributed to the persistence of a diffusive boundary layer above the substrate. Achieving monodisperse patterns requires (i) smooth, defect-free surfaces; (ii) operating within the diffusion-controlled regime to arrest nucleation events and set ψ_0 ($t \gg \tau_a$); and (iii) the inhibition of coalescence. Notably, forced or natural convection, induced by strong air injection or unstable air stratification, can impede the formation of the diffusive boundary layer near

the substrate, thus hindering the selection of ψ_0. This may explain the observed polydispersity when condensation occurs at vertical substrates [14,45] or below horizontal substrates [12,23,26,46]. Additionally, coalescence leads to bimodal distribution in drop sizes [15]. The few studies reporting monodisperse patterns confirm these requirements, focusing on defect-free, stably stratified liquid layers or liquid-infused substrates oriented horizontally [11,13,47], but these eventually evolve into polydisperse patterns due to coalescence. We show that the gel viscoelastic nature can effectively prevent coalescence, preserving monodispersity without affecting the universal late coarsening dynamics.

In conclusion, soft substrates hold great potential for achieving monodisperse, time-persistent breath figure patterns with tunable surface density that can extend to macroscopic scales. These patterns challenge the present understanding based on macroscopic elastocapillarity and serve as a probe for molecular pathways at polymeric interfaces.

Acknowledgments—The authors thank J. Scheefhals for supporting experiments, and acknowledge financial support from ANR (project APIEDS), NWO Vici (No. 680-47-632), and DFG (No. TH781/12 and No. SN145/1-1 within SPP 2171).

[1] K. Kelton and A. Greer, *Nucleation in Condensed Matter: Applications in Materials & Biology* (Elsevier, New York, 2010).
[2] D. Kashchiev, *Nucleation* (Elsevier, New York, 2000).
[3] L. Rayleigh, J. Röntgen Soc. **7**, 126 (1911), https://academic.oup.com/bjrrss/article-abstract/7/29/126/7647535.
[4] CM. Knobler, A. Steyer, P. Guenoun, and D. Fritter, Phase Transitions **31**, 219 (1991).
[5] D. Beysens, *The Physics of Dew, Breath Figures and Dropwise Condensation* (Springer, New York, 2022), Vol. 994.
[6] K. C. Park, P. Kim, A. Grinthal, N. He, D. Fox, J. C. Weaver, and J. Aizenberg, Nature (London) **531**, 78 (2016).
[7] J. Trosseille, A. Mongruel, L. Royon, MG. Medici, and D. Beysens, Eur. Phys. J. E **42** (2019).
[8] K. K. Varanasi, M. Hsu, N. Bhate, W. Yang, and T. Deng, Appl. Phys. Lett. **95**, 2007 (2009).
[9] P. B. Bintein, H. Lhuissier, A. Mongruel, L. Royon, and D. Beysens, Phys. Rev. Lett. **122**, 098005 (2019).
[10] B. J. Briscoe and K. P. Galvin, Colloids Surf. **56**, 263 (1991).
[11] A. Katselas, R. Parin, and C. Neto, Adv. Mater. Interfaces **9**, 1 (2022).
[12] R. N. Leach, F. Stevens, S. C. Langford, and J. T. Dickinson, Langmuir **22**, 8864 (2006).
[13] M. Sokuler, G. K. Auernhammer, M. Roth, C. Liu, E. Bonacurrso, and H. J. Butt, Langmuir **26**, 1544 (2010).
[14] A. Phadnis and K. Rykaczewski, Langmuir **33**, 12095 (2017).
[15] L. Stricker, F. Grillo, EA. Marquez., G. Panzarasa, K. Smith-Mannschott, and J. Vollmer, Phys. Rev. Res. **4**, L012019 (2022).
[16] S. Anand, K. Rykaczewski, S. B. Subramanyam, D. Beysens, and K. K. Varanasi, Soft Matter **11**, 69 (2015).
[17] C. S. Sharma, A. Milionis, A. Naga, C. W. E. Lam, G. Rodriguez, M. F. Del Ponte, V. Negri, H. Raoul, M. D'Acunzi, H. J. Butt, D. Vollmer, and D. Poulikakos, Adv. Funct. Mater. **32**, 2109633 (2022).
[18] A. Steyer, P. Guenoun, D. Beysens, and C. M. Knobler, Phys. Rev. B **42**, 1086 (1990).
[19] A. Steyer, P. Guenoun, and D. Beysens, Phys. Rev. E **48**, 428 (1993).
[20] D. Beysens and C. M. Knobler, Phys. Rev. Lett. **57**, 1433 (1986).
[21] J. L. Viovy, D. Beysens, and C. M. Knobler, Phys. Rev. A **37**, 4965 (1988).
[22] F. Family and P. Meakin, Phys. Rev. Lett. **61**, 428 (1988).
[23] M. Kolb, Phys. Rev. Lett. **62**, 1699 (1989).
[24] J. Blaschke, T. Lapp, B. Hof, and J. Vollmer, Phys. Rev. Lett. **109**, 068701 (2012).
[25] N. V. Brilliantov, Y. A. Andrienko, P. L. Krapivsky, and J. Kurths, Phys. Rev. E **58**, 3530 (1998).
[26] F. Family and P. Meakin, Phys. Rev. A **40**, 3836 (1989).
[27] R. W. Style, Y. Che, S. J. Park, B. M. Weon, J. H. Je, C. Hyland, G. K. German, M. P. Power, L. A. Wilen, J. S. Wettlaufer, and E. R. Dufresne, Proc. Natl. Acad. Sci. U.S.A. **110**, 12541 (2013).
[28] S. Karpitschka, A. Pandey, L. A. Lubbers, J. H. Weijs, L. Botto, S. Das, B. Andreotti, and J. H. Snoeijer, Proc. Natl. Acad. Sci. U.S.A. **113**, 7403 (2016).
[29] I. F. Guha, S. Anand, and K. K. Varanasi, Nat. Commun. **8**, 1 (2017).
[30] D. Baratian, R. Dey, H. Hoek, D. Van Den Ende, and F. Mugele, Phys. Rev. Lett. **120**, 214502 (2018).
[31] A. Böker, Y. Lin, K. Chiapperini, R. Horowitz, M. Thompson, V. Carreon, T. Xu, C. Abetz, H. Skaff, A. D. Dinsmore, T. Emrick, and T. P. Russell, Nat. Mater. **3**, 302 (2004).
[32] A. Zhang, H. Bai, and L. Li, Chem. Rev. **115**, 9801 (2015).
[33] F. J. Dent, D. Harbottle, N. J. Warren, and S. Khodaparast, ACS Appl. Mater. Interfaces **14**, 27435 (2022).
[34] B. Andreotti and J. H. Snoeijer, Annu. Rev. Fluid Mech. **52**, 285 (2020).
[35] See Supplemental Material at http://link.aps.org/supplemental/10.1103/PhysRevLett.134.188204 for details on condensation experiments on PDMS gels, g estimation, CNT derivation, and droplet detection methods.
[36] L.-H. Cai, T. E. Kodger, R. E. Guerra, A. F. Pegoraro, M. Rubinstein, and D. A. Weitz, Adv. Mater. **27**, 5132 (2015).
[37] R. Lhermerout, H. Perrin, E. Rolley, B. Andreotti, and K. Davitt, Nat. Commun. **7**, 12545 (2016).
[38] R. Lhermerout and K. Davitt, Colloids Surf. A **566**, 148 (2019).
[39] A. Bouillant, J. H. Snoeijer, and B. Andreotti, companion paper, Phys. Rev. Fluids **10**, 053605 (2025).
[40] A. Hourlier-Fargette, A. Antkowiak, A. Chateauminois, and S. Neukirch, Soft Matter **13**, 3484 (2017).
[41] M. Sokuler, G. K. Auernhammer, C. J. Liu, E. Bonaccurso, and H. J. Butt, Europhys. Lett. **89**, 36004 (2010).

[42] Y. O. Popov, Phys. Rev. E **71**, 036313 (2005).
[43] J. Merikanto, E. Zapadinsky, A. Lauri, and H. Vehkamäki, Phys. Rev. Lett. **98**, 145702 (2007).
[44] C. Li and R. Signorell, J. Aerosol Sci. **153**, 105676 (2021).
[45] J. W. Rose, Proc. Inst. Mech. Eng. Part A J. Power Energy **216**, 115 (2002).
[46] B. S. Sikarwar, S. Khandekar, S. Agrawal, S. Kumar, and K. Muralidhar, Heat Trans. Eng. **33**, 301 (2012).
[47] H. Zhao and D. Beysens, Langmuir **11**, 627 (1995).

Supplementary Material for 'Soft Condensation'

Ambre Bouillant,[1,2] Christopher Henkel,[3] Uwe Thiele,[3] Bruno Andreotti,[4] and Jacco H. Snoeijer[1]

[1] *Physics of Fluids Group, University of Twente, 7500 AE Enschede, Netherlands*
[2] *MSC, UMR 7057 CNRS, UPC, 10 rue A. Domon et L. Duquet, 75013, Paris, France*
[3] *Institut für Theoretische Physik, Universität Münster, W.Klemm-Str. 9, 48149 Münster, Germany*
[4] *LPENS, UMR 8550 CNRS, ENS, UPCité, SU, 24 rue Lhomond, 75005 Paris, France*

(Dated: May 13, 2025)

This supplementary material presents the procedure used to trigger condensation, as well as the substrate preparation and characterization protocols. We present the substrate rheological properties and specify the role of free polymer chains. We also detail the drop geometry (supporting the estimation of the function g for brush substrate) and provide an example of our droplet detection algorithm. For completeness, we provide the raw data and the corresponding fits mentioned in the manuscript.

CONDENSATION EXPERIMENTS

As schematized in Fig. 1 of the manuscript, the condensation chamber used herein is an axisymmetric 3D-printed box, with height $H = 42$ mm and inner diameter 80 mm, connected to two gas inlet on its upper part. Freshly prepared substrates are placed at the bottom of the chamber (in $z = H$) on a cooling stage (40 x 40mm Peltier element from RS Components, assisted by a heat sink).

Humidity control – We have developed a humidity regulator based on a PID controller driven by an Arduino microcontroller (available on this GitHub repository. A humidity sensor (DHT22 AM2302), placed near the chamber ceiling, measures the relative humidity $r_H^0 = P_v/P_{\rm sat}(T_0) < 1$, where P_v represents the vapour partial pressure in the air and $P_{\rm sat}(T_0)$ is the saturation/maximum value at the temperature T_0 (at the ceiling). The saturation pressure $P_{\rm sat}(T)$ can be derived analytically by integrating Clapeyron's relation between a state $[P_{\rm sat}(T), T]$ and the water boiling point, $[P_{\rm sat}(T_b) = P_0, T_b = 100°\text{C}]$, using the condensed phase approximation ($v_v >> v_\ell$) and assuming that vapor behaves as an ideal gas, ($P_{\rm sat} v_v = RT$):

$$\ln\left(\frac{P_{\rm sat}(T)}{P_{\rm sat}(T_b)}\right) = \frac{h_{\ell v}}{RT_b}\left(1 - \frac{T_b}{T}\right) \tag{1}$$

With $h_{\ell v} \approx 40.7$ kJ/mol, we get $h_{\ell v}/RT_b \approx 13.12$ and $h_{\ell v}/R \approx 4896$ K. We thus find a formula in close agreement with Rankine's semi-empirical formula involving the atmospheric pressure P_0, plotted in figure S1(a), that reads as

$$\ln\left(\frac{P_{\rm sat}(T)}{P_0}\right) = 13.7 - \frac{5120}{T} \tag{2}$$

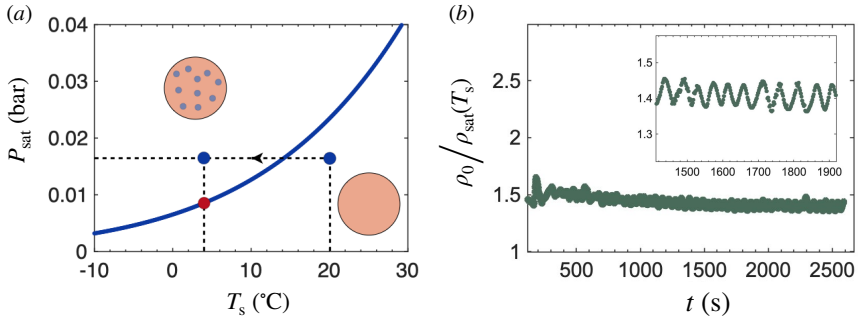

FIG. S1. (a) Saturation pressure $P_{\rm sat}$ with the substrate temperature T, from (2-1). Upon cooling, air can no longer carry the water content initially set, yielding condensation. (b) Humidity ratio $\rho_0/\rho_{\rm sat}(T_{\rm s})$, where ρ_0 is monitored and controlled at the ceiling ($z = H$) and $\rho_{\rm sat}(T_{\rm s})$ calculated on the substrate ($z = 0$) using 3 as a function of time. The inset zooms on oscillations.

Triggering condensation upon cooling – The relative humidity r_H^0 read at the ceiling ($z = H$, where $T_0 = 22 \pm 2°\text{C}$) is set to a targeted value beforehand by a valve connected a humid air inlet and remains controlled all along the experiment. The relative humidity hence oscillates by a few percent around the control value (Fig.S1(b)). Here, we express supersaturation in terms of vapor density rather than pressure to maintain consistency in our notation, particularly with the companion paper, where the vapor density field $\rho(r)$ is explicitly resolved. Denoting as ρ_0 the density of vapour molecules in air and $\rho_{\rm sat}(T_0)$ its saturation value at the temperature T_0 (taken at the ceiling), $r_H^0 = \rho_0/\rho_{\rm sat}(T_0) < 1$. The supersaturation degree is quantified by the difference in chemical potential $\Delta\mu = -k_B T \ln\left(\rho_0/\rho_{\rm sat}(T)\right)$ in the liquid and vapour phase. Since $P_{\rm sat}$ and $\rho_{\rm sat}$ are increasing functions of temperature (cf. Fig. S1(a), the supersaturation conditions ($\Delta\mu > 0$) can be achieved by cooling the substrate, while maintaining the pressure or air water content (P_v, ρ_0) fixed. Namely, starting with a homogeneous humidity (ρ_0), the relative humidity at the vicinity of the gel, cooled down to $T_s = 5 \pm 1°\text{C}$ within a few tens of seconds, is locally changed to

$$r_H = \frac{P_{\rm sat}(T_0)}{P_{\rm sat}(T_{\rm s})}\, r_H^0 = \exp\left(\frac{h_{\ell v}}{R}\left(\frac{T_0 - T_{\rm s}}{T_{\rm s}\, T_0}\right)\right) r_H^0 \tag{3}$$

Hence, a fast temperature quench triggers the condensation on the substrate. The nucleation and growth of water droplet is then recorded from above with a Nikon camera (D850), taking pictures every 10 s, mounted on a Olympus upright inverted microscope with $\times 50$ magnification. This yields a spatial resolution of 12 pixels/μm, allowing for the detection of droplets as small as a micron in size. To facilitate the detection, counting, and measurement of droplets, the image contrast is optimized by enlighting from the top.

SUBSTRATES PREPARATION AND CHARACTERIZATION

Substrate preparation – We prepare **soft, smooth reticulated PDMS polymer substrates** with elastic moduli ranging from ~ 100 Pa to ~ 1 MPa by mixing silicone (Dow Corning; Sylgard 184) with its reticulant agent in weight proportions ranging from 10:1 up to 80:1 (extending the range in [1]). The base polymer to cross-linker mass ratio r determines the cross-links density and the amount of free polymer chains that remain in the elastic network. The mixtures are weighed and shaped into Petri dishes.The millimetre-thick layers are then thoroughly degassed. To ascertain the gel homogeneity, smoothness and flatness, the reticulation reaction is first gently initiated at room temperature for $\sim$ 48h (on a stabilized optical table in a dust-free environment). Then, the samples are gently brought to 70°C in an oven (increasing the temperature by 1°C/min) and cured for 3h. Additional experiments were conducted using commercially available silicone elastomers, including polyvinylsiloxane (PVS, Elite Double 8, Zhermack) and another type of PDMS (CY52-276 A:B, Dow Corning). These elastomers were prepared by premixing their components in equal proportions for PVS and in relative proportions of 1.3:1 or 1:1 for the CY gels. It is worth noting that these gels were prepared near their stoichiometric ratios, resulting in a significantly lower amount of free oligomer chains compared to the softer Sylgard gels we tested. PVS cures within approximately 20 minutes at room temperature, whereas CY PDMS was cured following the same procedure as Sylgard 184 PDMS.
Experiments are also performed on **uncrosslinked PDMS (Sylgard 184) melt** and on **stiff PDMS pseudo-brushes** prepared following the grafting procedure described in [2, 3]. The grafted pseudo-brushes are nanometre-thick. With the PDMS chain lengths, immersion time and incubation temperature used, the pseudo-brushes are expected ti ve a few tens of nm thick, extrapolating data in [3], yielding an effectively stiff substrates inside which drops do no sink but form spherical caps of contact angle $\theta_{\text{brush}} = 100 \pm 5°$ (measured independently on macroscopic side-view images).

Substrate rheology – A portion of the preparations is sampled and cured under a rheometer (Anton Paar MCR502, parallel plate geometry, with plate diameter 50 mm) following the same curing procedure. Once cured, we probe the material viscoelasticity by running oscillatory shear tests at 20°C and at 5°C (with small strains). This yields the complex shear modulus G^* that can be convincingly fitted by the general function: $G'(\omega)+iG"(\omega) = G[1+(i\tau\omega)^n]$ to extract the shear modulus at long-time G, the relaxation time of the polymer τ and the exponent n reported in figures S2$(a-c)$ as a function of the ratio r of base polymer to cross-linker. Variations in r thus enables a fine tuning of the gel elastic modulus (from $\sim 10^2$ Pa to $\sim 10^6$ Pa) and of its viscoelastic properties. The gel viscous response can then be inferred by estimating the product $(G \times \tau)$, that has a constant value of 336 Pa.s that is consistent across all prepared gels, regardless of the polymer-to-crosslinker ratio r and mildly affected by temperature changes from 20 to 5°C.

We chose to label the different gels tested with their moduli G for three reasons: 1) it facilitates comparison among different gel types (such as PDMS from Sylgard or from Dow Corning and PVS elastomer), 2) it offers greater physical insight than r and 3) unlike other parameters as the geometrical factor g or the cross-linker spacing ξ, it can be measured unequivocally through independentdirect measurements.

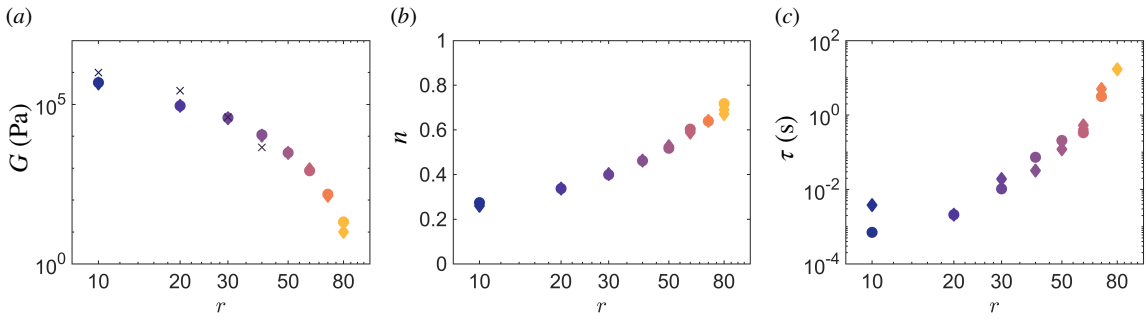

FIG. S2. Rheological properties of PDMS sample measured independently under a rheometer (Anton Paar MCR502, parallel plate). Fitting G^* with $G'(\omega)+iG"(\omega) = G[1+(i\tau\omega)^n]$ provides (a) the static shear modulus G, (b) the exponent n and (c) the viscoelastic relaxation time τ for different polymer-to-crosslinker ratio r. Measurement are done at 20°C (circles) and at 5°C (diamonds). Data from [1] are reproduced in panel a (as ×).

Typical distance bewteen crosslinks – From simple rubber elasticity theory (neglecting the contribution of entangled free chains), the elastic shear modulus is given by $G = 3k_BT\nu_x$, where ν_x is the density of crosslinks in the elastomer network. Therefore, the typical distance between crosslinks, $\xi_x \sim \nu_x^{-1/3}$, scales as $\xi_x \sim (3k_BT/G)^{1/3}$, which

ranges from ∼2 nm to 100 mm for the tested gels as G is decreased from 10^6 Pa (corresponding to $r = 10$: 1) down to 10 Pa, ($r = 80$: 1). Note that since $\psi_0 \sim G^{-1/2}$, $\psi_0 \sim \left(\xi^3/3k_BT\right)^{1/2}$. Consequently, the droplet density ψ_0 increases as the crosslinker concentration decreases, corresponding to looser crosslinked networks with larger ξ_x. Paradoxically, fewer crosslinks and more free chains lead to the formation of more nucleated droplets. This rules out the possibility that crosslinks serve as nucleation-promoting heterogeneous sites.

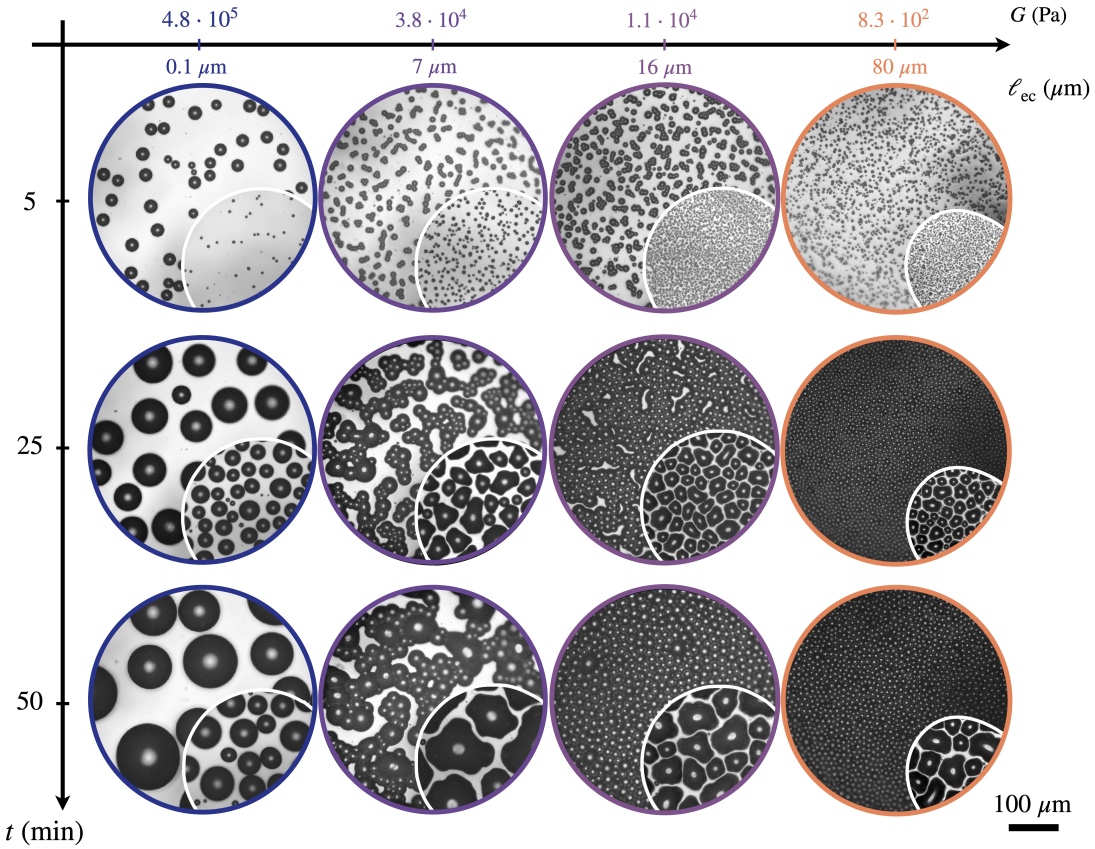

FIG. S3. Breath figures obtained on regular gels (main panels) and on gels whose free chains were extracted following the procedure described in [4] (bottom right panels). The scale bar corresponds to 100 μm for the main panels (regular gels) and to 200 μm for the bottom right insets.

Extracting the gels free polymer chains – To check the influence of the free uncross-linked chain on the nucleation and condensation dynamics, we have reproduced condensation experiments on washed gels. To that end, we extract free polymer chains from PDMS samples by using toluene as a swelling solvent, following the procedure developed by Hourlier-Fargette [4]. Each sample is weighted before and after the washing procedure to ensure the total removal of the uncrosslinked chains (from 3% of the total weight of our PDMS samples up to 100% for the most extreme case, in line with [1]).

FIG. S3 compares the top-viewed breath figures obtained for regular and washed gels (as the bottom right inserted panels). We find that on washed gels, the droplet surface density measured at the **early stage of condensation** still increases when decreasing the polymer-to-cross-linker ratio r, the effect being even more pronounced for the softer washed gels. Note that the temporal correspondence of the inserts with the main panels of FIG. S3 is not exact (±2 min) as images were selected to ensure that droplets are optically resolved. Hence, size comparison cannot be made on those images. We thus find that the surface density selection (ψ_0) is barely affected by the presence of free chains. However, several changes can be noted on washed gels during the **later stages of breath figure evolution**. First, viscous dissipation is much reduced, so Cheerios interactions are less hindered, leading to immediate droplet coalescence upon contact. The extra delay in pattern coarsening observed on soft viscoelastic gels is suppressed ($\tau_p \approx 0$) so droplets become larger, fewer and polydispersed. Additionally, droplet shapes no longer remain spherical, which betrays the presence of adhesion and contact angle hysteresis on free-chain free PDMS samples.

MACROSCOPIC DESCRIPTION OF THE DROP GEOMETRY AND THE ENERGY BARRIER

We specify here the shape of a drop sitting on a solid or a liquid (function of the surface energies γ, $\gamma_{s\ell}$ and γ_{sv} of the liquid/vapor, solid/liquid and solid/vapor interfaces) and the associated macroscopic energy barrier to nucleate. **On a rigid substrate,** the drop adopts a spherical cap shape with radius of curvature κ^{-1} and horizontal radius R (cf. Fig. S4). It meets its substrate with a contact angle θ with respect to the horizontal, which follows Young's law:

$$\gamma \cos\theta_Y = (\gamma_{sv} - \gamma_{s\ell}) \tag{4}$$

Since $R = \kappa^{-1}\sin\theta$ and $\kappa^{-2} = R^2 + (\kappa^{-1} - h)^2$, the interfaces area are $S_{\ell v} = \frac{2\pi R^2}{(1+\cos\theta)}$; $S_{s\ell} = \pi R^2$ and volume is

$$V = R^3 g(\theta) \quad \text{with} \quad g(\theta) = \frac{\pi}{3}\frac{(2+\cos\theta)(1-\cos\theta)^2}{\sin^3\theta} \tag{5}$$

where the function g modulates the effect of the substrate wetting properties as shown in Fig. S4(b) in blue. Balancing the energy penalties $\Delta\Phi_{\text{surface}} = \gamma S_{\ell v} + \gamma_{s\ell} S_{s\ell} - \gamma_{sv}\pi R^2$ with the energy available due to supersaturation $\Delta\Phi_{\text{bulk}} = \rho_\ell V/m_0 \Delta\mu$ (m_0 being the mass of a molecule and ρ_ℓ the liquid density), the energy variation writes as:

$$\Delta\Phi = \left(3\sin\theta\gamma R^2 g(\theta) - \frac{V\rho_\ell}{m_0} kT\Lambda\right) \quad \text{with} \quad \Lambda = \ln\left(\frac{\rho_0}{\rho_{\text{sat}}}\right) \tag{6}$$

On a liquid, the shape of a drop is that of a floating lens as illustrated in the top right schematic in Fig S4. The liquid/air interface forms an angle θ above the horizontal, while the drop sinks into the substrate with an angle θ'. The angles θ and θ' are twined by Neumann's laws:

$$\gamma\cos\theta + \gamma_{s\ell}\cos\theta' = \gamma_{sv} \quad \text{and} \quad \gamma\sin\theta - \gamma_{s\ell}\sin\theta' = 0 \tag{7}$$

Solving this system with $\gamma_{sv} = 22$ mN/m, $\gamma_{lv} = 70$ mN/m, $\gamma_{sl} = 51.5$ mN/m, we predict the equilibrium angles θ and θ' of a water lens on liquid PDMS (Fig.S4(a)). We now can write the area of the liquid/vapour and solid/vapour interfaces in term of θ or θ' as before, as well as the drop total volume

$$V = \frac{\pi}{3}R^3\Big[g(\theta) + g(\theta')\Big] \equiv \frac{\pi}{3}R^3 g \tag{8}$$

where g is plotted in Fig. S4(b) in orange for θ' at equilibrium and in blue imposing $\theta' = 0$ (drop do not sink). Balancing the energy penalties with the supersaturation energy yields an energy variation

$$\Delta\Phi = \left(\gamma\pi\sin\theta R^2\Big(g(\theta) + g(\theta')\Big) - \frac{V\rho_\ell}{m_0} kT\Lambda\right) \tag{9}$$

$\Delta\Phi(R)$ admits a maximum, specifying the energy barrier $\Delta\Phi^*$ and the nanometer-scale critical nucleus size R^*.

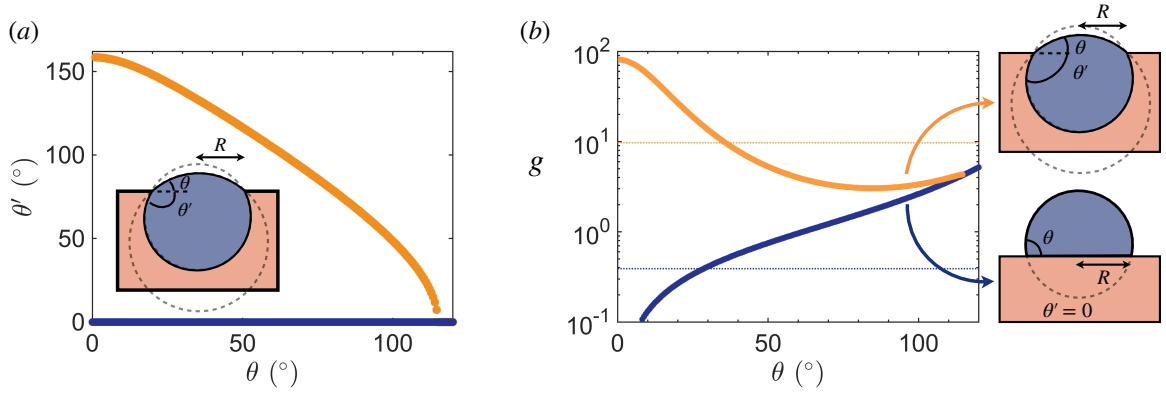

FIG. S4. (a) Drop sinking angle θ' predicted as a function of the upper contact angle θ, assuming a macroscopic equilibrium and solving Neumann's system with $\gamma_{sv} = 22$ mN/m, $\gamma_{lv} = 70$ mN/m, $\gamma_{sl} = 51.5$ mN/m. (b) Geometrical factor $g \equiv V/R^3$ as a function of θ predicted for θ' at macroscopic equilibrium (orange curve) or for $\theta' = 0$ (drops do not sink into the gel).

Contact angle independant macroscopic measurements – On brush substrates, we measured on independent side-view experiments a contact angle value $\theta_{\rm brush} = 100 \pm 5°$. Hence, the corresponding geometric function $g = 2.6 \pm 0.4$. On soft PDMS gels, independent side-view macroscopic measurements showed that the upper contact angle θ varies both with the ratio $\ell_{\rm ec}/R$ and with time. Figure S5 reveals a continuous transition for θ from stiff to soft substrates as $\ell_{\rm ec}/R$ increases and the drop grows. The sinking angle θ' cannot be accessed in those experiments but it also varies with time, adjusting to θ and as the droplet gradually sinks into the gel. As a result, neither the contact angles θ, θ' nor the geometrical factor remain constant, making g difficult to predict. Therefore, we fitted g rather than imposing it (as shown in Fig. 3).

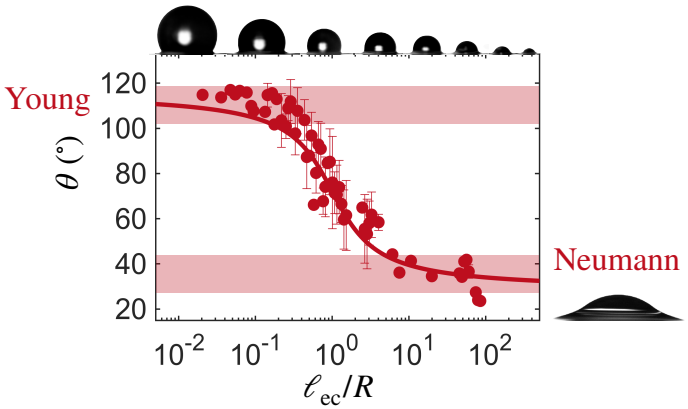

FIG. S5. Upper contact angle θ measured on independent side-view macroscopic experiments, as a function of the ratio $\ell_{\rm ec}/R$. A water droplet is deposited within a few seconds onto PDMS gels (prepared with polymer-to-crosslinker ratios r from 10:1 to 80:1) using a piezo-driven pipette (AD-K-501, Microdrop Technologies). This allows precise control of the droplet radius from 30 μm to 500 μm. The red line represents a fit to the equation $\theta = \theta_a - \theta_b \times \arctan\left[\log\left(\ell_{\rm ec}/R\right)\right]$, with $\theta_a \approx 72°$ and $\theta_b \approx 28°$.

Since drops nucleate at a nanometric scale, $R^* << \ell_{\rm ec}$ for all the tested gels (even the stiffer gel, for r = 10:1). Hence, elasticity is marginal and the elastic energy associated to the formation of the elastocapillary ridge or the sinking of a drop are both vanishing. The condensing vapors are expected to encounter a polymer melt and nucleate with an upper contact $\theta \sim 30°$. However, the value of θ' remains unknown and can only be estimated assuming macroscopic equilibrium (Neumann's law), an assumption that heavily relies on the premise that droplets can deform their substrates within the nucleation timescale.

Energy barrier – The geometric-part of the normalized energy barrier χ, defined as $\chi = \ln^2\left(\rho/\rho_{\rm sat}\right) \Delta\Phi^*/k_BT$ is

$$\chi \equiv \frac{4\pi}{3}\left(\frac{\gamma}{k_BT}\right)^3\left(\frac{m_0}{\rho_\ell}\right)^2\Big(g(\theta)+g(\theta')\Big)\sin^3\theta \tag{10}$$

χ can be estimated at macroscopic equilibrium in the two limits: 1) on rigid brush substrates, $\theta_{\rm brush} = 100 \pm 5°$ ($\theta' = 0$), which yields $\chi_{\rm brush} = 59 \pm 6$; 2) on soft PDMS gels, where $\chi = 40 \pm 6$ assuming the elastocapillary macroscopic framework holds for nanometric droplets – $\theta = 30 \pm 5°$ and $\theta' = 138 \pm 6°$ (Neumann's law, cf. orange curve in Fig. S4(a)). The nucleation quantities for PDMS melts and PDMS brushes are summarized in Table . To

	θ	θ'	χ (theory)	χ(fitted)	J_0(fitted)
PDMS melt satisfying Neumann's law	30 ± 5 °	138 ± 6 °	40 ± 6	1.3	2.9×10^{12} m^{-2}.s^{-1}
PDMS rigid brush satisfying Young's law	100 ± 5 °	0°	59 ± 6	~ 0	10^{15} m^{-2}.s^{-1}

TABLE I. Summary of the quantities used to compare χ between experiments and macroscopic estimates of the energy gap, obtained using $\gamma = 70$ mN/m; $k_BT = 3.8 \times 10^{-21}$ J; $m_0 = 2.99 \times 10^{-26}$ kg; $\rho_\ell = 1000$ kg/m^3; $\rho_{\rm sat} = 5 \times 10^{23}$ m^{-3}.

compare the experimental results with the theory based on a macroscopic reaction path, we need to assume that the inversion between the measurement of ψ_0 and the nucleation rate J is correctly modeled. The fitted values of J_0 and χ rely on a reasonable parametrization of the energy gap. We provide in the table below the values of J obtained for a typical humidity level. Regarding the macroscopic theory, it assumes a model for the attempt frequency per unit area J_0. The upper bound of any model for J_0 is the collision frequency of water molecules in the vapor phase.

$$J_0 = \frac{1}{4}\rho\langle v\rangle \quad \text{with} \quad \langle v\rangle = \sqrt{\frac{8\pi k_BT}{m_0}} \tag{11}$$

This overestimation of J_0 does not compensate for the exceedingly small order of magnitude of the Boltzmann factor $\exp(-\chi/\Lambda^2)$ for values of χ in the range of several tens.

$J = J_0\ \exp\left(-\chi/\Lambda^2\right)$	J(macro)	J(fitted)
PDMS melt satisfying Neumann's law	$10^{-333}\,\mathrm{m}^{-2}.\mathrm{s}^{-1}$	$13\ \mathrm{m}^{-2}.\mathrm{s}^{-1}$
PDMS rigid brush satisfying Young's law	$10^{-503}\,\mathrm{m}^{-2}.\mathrm{s}^{-1}$	$10^{15}\ \mathrm{m}^{-2}.\mathrm{s}^{-1}$

TABLE II. Comparison of the nucleation rate predicted by macroscopic theory (with $\langle v\rangle = 569$ m/s) and the rate deduced by fitting experimental data, for $\rho/\rho_{\mathrm{sat}} = 1.25$ and $\Lambda \approx 0.22$.

DETECTING AND COUNTING DROPLETS

We use the open-source software Cell Profiler to detect, count and measure the drop characteristics over time. On soft gels, *i.e.* provided $R \sim \ell_{\mathrm{ec}}$, drops gather into clusters. To properly count them, we first detect the clusters of drops and then, among it, we look for the dark spot at the summit of each drops that corresponds to the light reflection, to segment around it. The matlab base software helps adjusting the detection and segmentation parameters throughout the growth dynamics in a practical and visual way. The results of this detection are illustrated in figure S6.

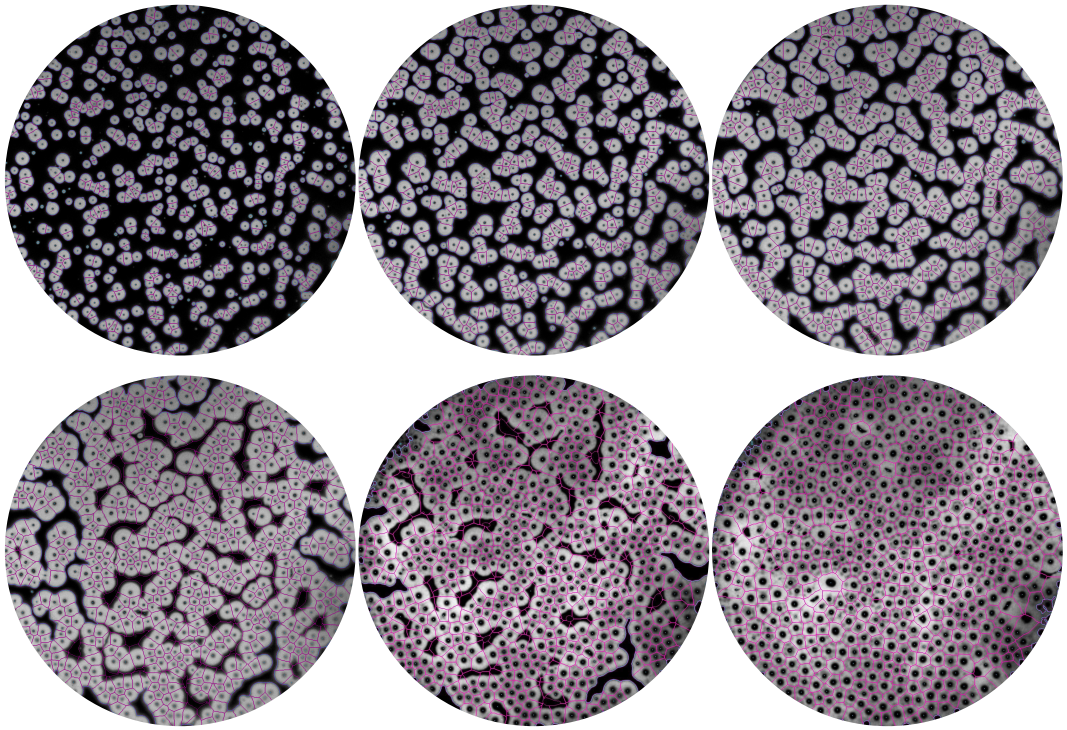

FIG. S6. Detection of droplets along the condensation dynamics. on a soft gels. The contrast has been enhanced and inverted. Using Cell Profiler, we first detect clusters of drops and then look for the dark spot at the summit of each drops that corresponds to the light reflection to segment around it. The results of this segmentation is shown in magenta. We export the individual size, shape descriptor and coordinate of individual drops to get statistics.

RAW DATA AND FIT

For completeness, we provide here the raw data and the corresponding fits mentioned in the manuscript. We recall the mean collected volume expression

$$V \equiv gR^3 = \frac{3m_0 D_0}{\pi \rho_\ell H \rho_{\rm sat}} \left(\frac{\rho}{\rho_{\rm sat}} - 1 \right) \frac{t}{\psi} \tag{12}$$

where $H \sim 42$ mm, $m_0 = 2.99 \times 10^{-26}$ kg, $D_0 = 2.3 \times 10^{-5}$ m^2/s, ρsat $= 5 \times 10^{23}$ m^{-3} and $\rho_\ell = 10^3$ kg/m^3).

On PDMS brushes – We have quantified the droplet number surface density ψ (Fig. S7(a)) and the droplet mean radius $\bar{R}$ as time goes on (Fig. S7(b)).

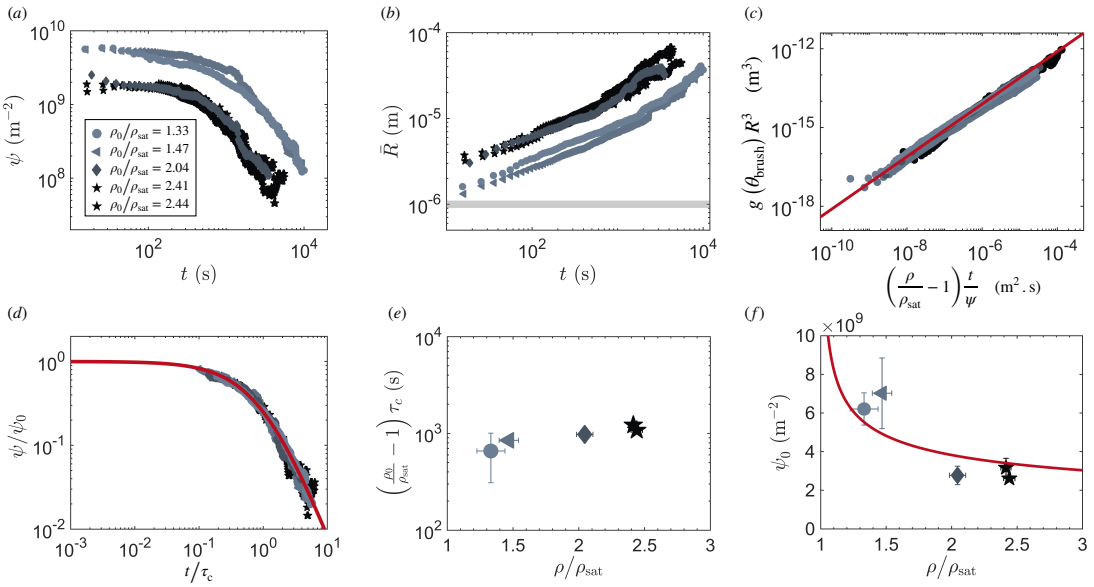

FIG. S7. Data for PDMS brushes obtained for different humidity conditions. (a) Droplet surface density ψ and (b) mean droplet radius $\bar{R}$ as a function of time t. The grey line indicates the resolution limit. (c) Mean volume collected per droplet $\bar{V} \equiv g(\theta_{\rm Brush})R^3$ where the function $g(\theta_{\rm Brush}$, defined in eq. 5, is calibrated on independent side-view experiments $\theta_{\rm brush} = 100 \pm 5°$. The red line is the theoretical prediction (12) plotted without any adjusting parameter. (d) Droplet number surface density normalized by its initial value ψ/ψ_0 as a function of t/τ_c, showing the coalescence-driven coarsening dynamics. The value of τ_c, extracted by fiting the data with the law $\psi/\psi_0 = \left[1 + t/\tau_c\right]^{-2}$, is plotted in panel e as a function of the relative humidity. (f) Initial droplet density as a function of the relative humidity. Data are fitted with equation (3) of the main text. yielding $J_0 = 3.5 \times 10^{15}$ m^{-2}.s^{-1} and $\chi \approx 0$.

Using the contact angle value measured on independent side-view experiments, $\theta_{\rm brush} = 100 \pm 5°$, the collected volumes are found to closely agree with our theoretical prediction (Fig S7(c)). The coarsening dynamics obeys a universal law well described by $\psi/\psi_0 = \left[1 + t/\tau_c\right]^{-2}$ (Fig S7(d)), with a coarsening time that scales as $\tau_c \sim \left(\rho/\rho_{\rm sat} - 1\right)^{-1}$ as shown in Fig S7(e). Fitting our initial droplet density ψ_0 using equation (3) of the main text provides values for the nucleation attempt rate $J_0 = 3.5 \times 10^{15}$ m^{-2}.s^{-1} and an effective energy barrier $\chi \approx 0$.

On PDMS soft gels – The detection and fitting procedures have been reproduced for a soft gel, with softness $\ell_{\rm ec} = 7$ μm, $G = 1.1 \times 10^4$ Pa and for five different humidity ratio $\rho_0/\rho_{\rm sat}$. Data are presented in figure S8. We verify that the mean collected volume still increase linearly with $\left(\rho/\rho_{\rm sat} - 1\right)\, t/\psi$ (as predicted in 12); that the number of drops evolves according to the coarsening law similar that for the stiff case but corrected by a delay time $\tau_{\rm p} \sim 10^3$ s. The fit for ψ_0 versus humidity provides values for the nucleation attempt rate $J_0 = 2.9 \times 10^{12}$ m^{-2}.s^{-1} and the energy barrier effectively felt at nucleation $\chi \approx 1.3$.

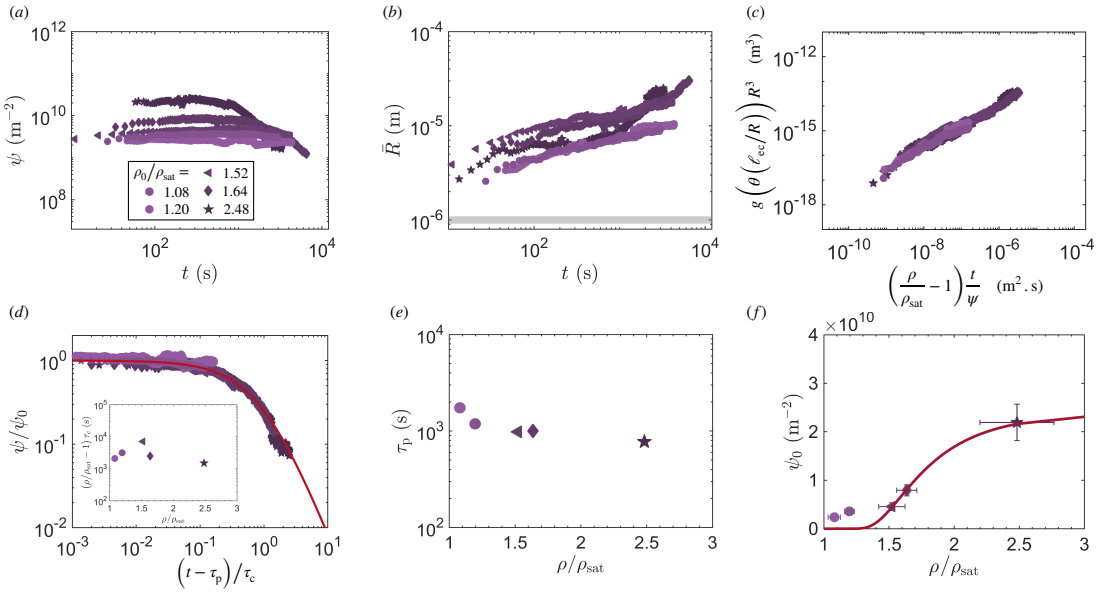

FIG. S8. Data for PDMS gels with softness $\ell_{ec} = 7\ \mu$m, $G = 1.1 \times 10^4$ Pa obtained for five different humidity ratio ρ_0/ρ_{sat}.(a) Droplet surface density ψ and (b) mean droplet radius $\bar{R}$ plotted as a function of time t. (c) Mean volume collected per droplet $\bar{V} \equiv g(\theta)R^3$ where $g(\theta)$ is let as a free parameter (fitted value shown in inset and in Fig.3). (d) ψ/ψ_0 versus $(t-\tau_p)/\tau_c$, showing the coarsening dynamics owing to coalescence. τ_c and τ_p extracted for the fit $\psi/\psi_0 = \left[1+(t-\tau_p)/\tau_c\right]^{-2}$ are presented in the inset and on panel (e) respectively as a function of the relative humidity. (f) Initial droplet density ψ_0 as a function of the relative humidity. Data are fitted with equations (3) of the main text yielding $J_0 = 2.9 \times 10^{12}$ m^{-2}.s^{-1} and $\chi \approx 1.3$.

The detection and fitting procedures have been also performed for our data set for constant humidity ratio ($\rho_0/\rho_{sat} = 1.22 \pm 0.11$) and varying gel elastic modulus G, as presented in figure S9.

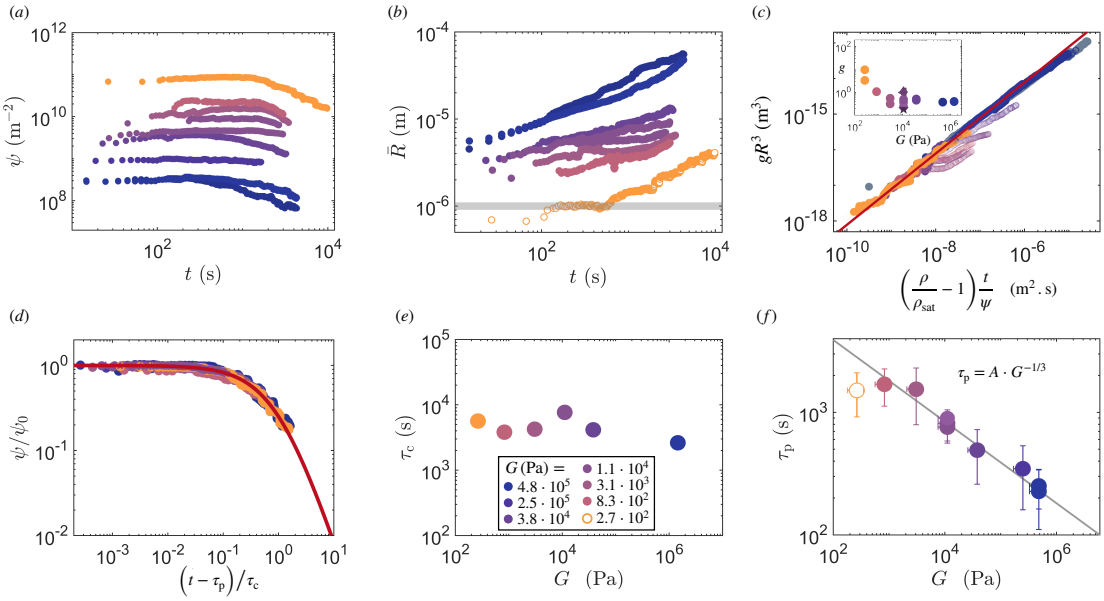

FIG. S9. Data for soft PDMS obtained for $\rho_0/\rho_{sat} = 1.22 \pm 0.11$ and varying substrate elastic modulus G from 4.8×10^5 Pa for the stiffer (blue) down to 2.7×10^2 for the softer (blue), see the color label common to all plots in panel (e). (a) Droplet surface density ψ and (b) mean droplet radius $\bar{R}$ plotted as a function of time t. (c) Mean volume collected per droplet $\bar{V} \equiv g(\theta)R^3$ where the function $g(\theta)$ is let as a free parameter, displayed in the inset. (d) Droplet number surface density normalized by its initial value ψ/ψ_0 as a function of $(t-\tau_p)/\tau_c$, showing the coarsening dynamics despite the reluctance to coalesce. τ_c and τ_p extracted for the fit $\psi/\psi_0 = \left[1+(t-\tau_p)/\tau_c\right]^{-2}$ are presented on panels (ef), respectively, as a function of G. τ_c is independant of G while $\tau_p = A \times G^{-1/3}$, with $A = 18130$ s.m$^{1/3}$.kg$^{-1/3}$.

[1] L.-H. Cai, T. E. Kodger, R. E. Guerra, A. F. Pegoraro, M. Rubinstein, and D. A. Weitz, Advanced materials **27**, 5132 (2015).
[2] R. Lhermerout, H. Perrin, E. Rolley, B. Andreotti, and K. Davitt, Nat. Commun. **7**, 12545 (2016).
[3] R. Lhermerout and K. Davitt, Colloids and Surfaces A: Physicochemical and Engineering Aspects **566**, 148 (2019).
[4] A. Hourlier-Fargette, A. Antkowiak, A. Chateauminois, and S. Neukirch, Soft Matter **13**, 3484 (2017).